JOURNAL OF GEOPHYSICAL RESEARCH, VOL. 108, NO. D2, 4051, doi:10.1029/2002JD002095, 2003

# Hemispheric differences in the temperature of the summertime stratosphere and mesosphere

David E. Siskind, Stephen D. Eckermann, and John P. McCormack
E. O. Hulburt Center for Space Research, Naval Research Laboratory, Washington, D. C., USA

M. Joan Alexander
Colorado Research Associates, Boulder, Colorado, USA

Julio T. Bacmeister
Goddard Earth Sciences and Technology Center, University of Maryland, Baltimore County, Baltimore, Maryland, USA

Received 15 January 2002; revised 12 August 2002; accepted 13 August 2002; published 22 January 2003.

[1] We study two processes which may govern interhemispheric differences in the temperature of the summertime middle atmosphere. The first is the direct radiative effect arising from the eccentricity of Earth's orbit. The second factor is the difference in gravity-wave filtering due to the hemispheric asymmetries in the summertime mean winds of the troposphere and lower stratosphere. Using two different gravity-wave drag parameterizations and a zonal wind climatology, we find greater gravity wave induced acceleration of the zonal flow in the southern summer lower stratosphere, which leads to weaker gravity wave drag in the southern upper mesosphere. Using a two-dimensional chemical-dynamical model, we evaluate the temperature changes caused by these drag differences and compare them with those caused by direct radiative asymmetry. The radiative asymmetry peaks in the upper stratosphere but is nonnegligible between 20 and 80 km. The dynamical asymmetry has a primary contribution in the upper mesosphere and a secondary contribution in the lower stratosphere. Overall, our results support the idea that poleward of 30° the southern middle atmosphere is warmer than the north by 3–8K between 20 and 85 km. As a result, our model suggests that the relative humidity of the northern summer mesopause region is greater than in the south. This implies that mesospheric clouds (PMCs and NLCs) should be more frequent and more extensive in the north than in the south. *INDEX TERMS:* 3332 Meteorology and Atmospheric Dynamics: Mesospheric dynamics; 3329 Meteorology and Atmospheric Dynamics: Mesoscale meteorology; 3334 Meteorology and Atmospheric Dynamics: Middle atmosphere dynamics (0341, 0342); 3384 Meteorology and Atmospheric Dynamics: Waves and tides; *KEYWORDS:* mesosphere, stratosphere, gravity waves, polar mesospheric clouds, temperature

**Citation:** Siskind, D. E., S. D. Eckermann, J. P. McCormack, M. J. Alexander, and J. T. Bacmeister, Hemispheric differences in the temperature of the summertime stratosphere and mesosphere, *J. Geophys. Res.*, *108*(D2), 4051, doi:10.1029/2002JD002095, 2003.

## 1. Introduction

[2] Over the past 15 years, there have been numerous studies comparing the Northern and Southern middle atmospheres. Most of these studies have focused on winter conditions in the stratosphere and have been motivated by the need to understand why an ozone hole exists in the Southern Hemisphere (SH) but not in the Northern Hemisphere (NH). It is now generally understood that the SH winter stratosphere is colder than its NH counterpart due to weaker planetary-wave activity in the SH [e.g., *Garcia et al.*, 1992], a result ultimately attributable to the weaker topographic forcing in the SH. Much less attention has been devoted to summertime conditions. One recent exception was *Rosenlof* [1996]. Using several sources of data, including MSU-4 satellite data, the National Meteorological Center (NMC, now known as the National Center for Environmental Prediction, NCEP) analysis and United Kingdom Meteorological Office (UKMO) assimilation, she showed that the SH summer stratosphere is consistently warmer than the NH for latitudes poleward of 30–40°. While an obvious cause of this summertime temperature difference might be the fact that Earth is closer to the Sun in January than July, *Rosenlof* [1996] showed that differing dynamics also likely plays a role. Specifically, *Alexander and Rosenlof* [1996] showed that the differences in the mean zonal wind shear between the NH and SH lead to greater gravity wave induced forcing in southern summer. The differing Eliasen-Palm (EP) flux divergences from


0148-0227/03/2002JD002095$09.00

# Report Documentation Page

*Form Approved*
*OMB No. 0704-0188*



| 1. REPORT DATE | 2. REPORT TYPE | 3. DATES COVERED |
|---|---|---|
| **12 AUG 2002** | | **00-00-2002 to 00-00-2002** |

| 4. TITLE AND SUBTITLE | 5a. CONTRACT NUMBER |
|---|---|
| **Hemispheric differences in the temperature of the summertime stratosphere and mesosphere** | 5b. GRANT NUMBER |
| | 5c. PROGRAM ELEMENT NUMBER |
| 6. AUTHOR(S) | 5d. PROJECT NUMBER |
| | 5e. TASK NUMBER |
| | 5f. WORK UNIT NUMBER |
| 7. PERFORMING ORGANIZATION NAME(S) AND ADDRESS(ES) **Naval Research Laboratory,E.O. Hulburt Center for Space Research,Washington,DC,20375** | 8. PERFORMING ORGANIZATION REPORT NUMBER |
| 9. SPONSORING/MONITORING AGENCY NAME(S) AND ADDRESS(ES) | 10. SPONSOR/MONITOR'S ACRONYM(S) |
| | 11. SPONSOR/MONITOR'S REPORT NUMBER(S) |

12. DISTRIBUTION/AVAILABILITY STATEMENT
**Approved for public release; distribution unlimited**

13. SUPPLEMENTARY NOTES

14. ABSTRACT

15. SUBJECT TERMS

| 16. SECURITY CLASSIFICATION OF: | | | 17. LIMITATION OF ABSTRACT | 18. NUMBER OF PAGES | 19a. NAME OF RESPONSIBLE PERSON |
|---|---|---|---|---|---|
| a. REPORT **unclassified** | b. ABSTRACT **unclassified** | c. THIS PAGE **unclassified** | **Same as Report (SAR)** | **13** | |

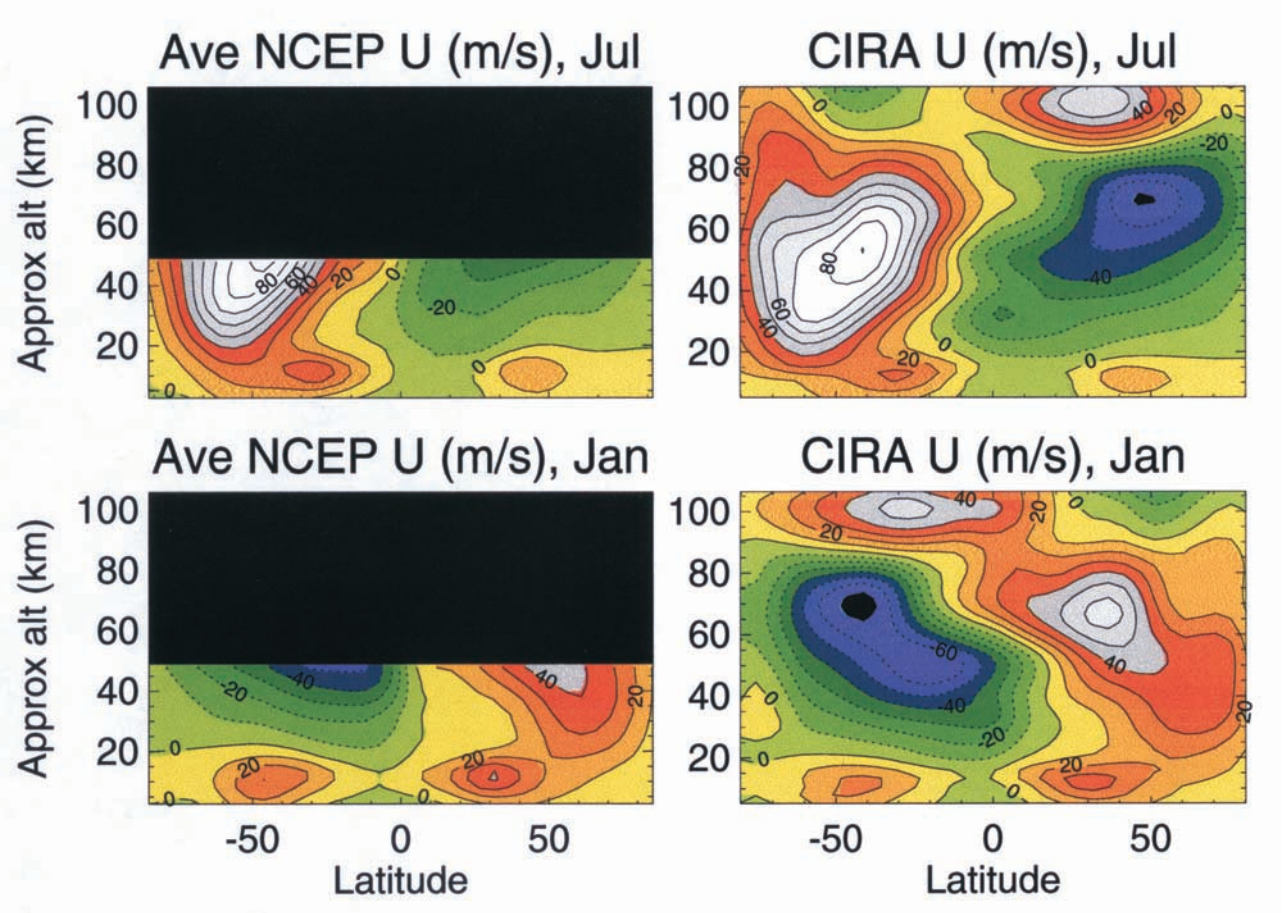


**Figure 1.** Zonal wind climatologies from CIRA and NCEP for July and January.

these waves drive a stronger residual circulation in southern summer relative to northern summer which yields more adiabatic heating via increased descent. To date however, the relative roles of gravity-wave drag and orbital eccentricity have not yet been quantified in a global atmospheric model.

[3] In contrast to the stratosphere, no equivalently well validated global temperature data set for the mesosphere exists to allow assessments of north-south differences This is unfortunate because N-S temperature differences, particularly in summertime, have recently become of great interest. Several mesospheric data sets have provided preliminary indications of N-S asymmetries, though not all of the findings are consistent. Specifically, *Woodman et al.* [1999] discuss N-S differences in the occurrence of Polar Mesospheric Summer Echoes (PMSEs). PMSEs are measured by VHF radars, near the mesopause at high latitude summer, and are believed to result from enhanced backscatter from narrow layers of charged ice aerosols. *Woodman et al.* [1999] suggested that the difficulties they encountered in observing SH PMSEs may be because the upper mesosphere in southern summer is warmer than in northern summer, thus limiting the formation of subvisible ice particles. To explain these differences, they suggested that the Antarctic mesopause is about 7.5K warmer in January than the Arctic in July. A concurrent review of several temperature measurements of the mesopause by *Huaman and Balsley* [1999] also led them to conclude that the austral summer was warmer than the boreal summer at mesopause altitudes.

[4] Radar wind measurements of *Vincent* [1994] and most recently, *Dowdy et al.* [2001] support the above suggestions. They found that meridional winds over Alaska in July are stronger than over Antarctica in January. Furthermore the net variance in the zonal wind field was greater in NH summer relative to SH summer which they interpreted in terms of greater gravity-wave activity in the NH summer relative to the SH. Since the existence of the cold summer mesopause is linked to the mean meridional circulation which, in turn, is driven by gravity-wave breaking, one would expect a stronger circulation in July relative to January if the NH summer were colder than the SH. On the other hand, *Lubken et al.* [1999] report a series of rocket measurements over Antarctica and concluded that any N-S temperature difference was much smaller, within 3K in January relative to July. Other relevant data include ground-based observations of noctilucent clouds (NLCs) or their global manifestation, polar mesospheric clouds (PMCs). Since the brightness of these clouds is very sensitive to temperature, even a small N/S temperature difference should show up as a large difference in cloud brightness. To date, no systematic hemispheric difference in mesospheric cloud brightness or occurrence frequency has been reported. *Chu et al.*

[2001] report that the height of PMCs over the South Pole is /*sim*2–4 km higher than that over the North Pole and suggest it results from stronger upwelling over the South Pole. This would imply colder temperatures over the South Pole, in conflict to the inferences from radar and PMSE observations. On the other hand, satellite data from *Carbary et al.* [1999] and *Thomas and Olivero* [1986] do not agree with the lidar data.

[5] In light of the above observational limitations as well as the general lack of theoretical study of this problem, it is useful to investigate some of the atmospheric processes which may play a role in generating N-S differences in the summer mesosphere. In this paper, we do this in two ways. First, in section 2, we calculate and compare gravity wave induced drag fields using two gravity-wave drag parameterizations and climatological wind fields. Then, in section 3, we incorporate one of these parameterizations in a coupled two-dimensional chemical/dynamical model of the middle atmosphere to simulate N/S differences in temperature and water vapor. Finally, (section 4) we separate out the relative roles of radiative and dynamical effects in producing hemispheric differences.

## 2. Analysis of Climatology

[6] One theme common to the data sets discussed above is that in all cases the geographic and temporal coverage is limited and the uncertainties are large. By contrast, detailed and reasonably reliable temperature and wind climatologies do exist for the troposphere and stratosphere. Since the climate of the troposphere and stratosphere is much better established than that of the mesosphere, it is useful to consider how N-S differences in the atmosphere below 50 km might impact conditions at higher altitudes. In this section we use an atmospheric climatology of mean winds and temperature along with two gravity-wave drag parameterizations to evaluate these effects.

### 2.1. Overview

[7] Figure 1 presents the zonal winds for July and January from two well known atmospheric climatologies, the COSPAR International Reference Atmosphere (CIRA) [*Fleming et al.*, 1990] and a climatology derived from the National Center for Environmental Prediction (NCEP) analyses [*Randel*, 1992]. Both climatologies show consistent features in the altitude regime where they overlap. There is a strong westerly jet at the winter stratopause which is significantly stronger in the SH (July) than in the NH (January). This difference has been modeled by *Garcia et al.* [1992]. In summer, the stratospheric winds are easterly and are stronger in January than July, most notably in the NCEP climatology. Consistent N-S differences are present at lower altitudes. Thus the tropospheric westerlies are stronger in winter than in summer and stronger in southern summer than in northern summer. The net effect of the stronger January stratospheric easterlies and tropospheric westerlies is a larger vertical shear in the January zonal wind profile than in July. This has been discussed by *Alexander and Rosenlof* [1996] in the context of the stratospheric summer. Since only the CIRA data span the complete altitude regime of interest, in the rest of this section, we will rely exclusively on the CIRA climatology in comparing the results of two gravity-wave models.

**Table 1.** Summary of Gravity-Wave Parameters

| Phase Speed, m/s | Launch Amplitude, m |
|---|---|
| 0 | 250 |
| +10 | 150 |
| −10 | 150 |
| +20 | 100 |
| −20 | 100 |
| +30 | 50 |
| −30 | 50 |
| +40 | 25 |
| −40 | 25 |
| +50 | 15 |
| −50 | 15 |

### 2.2. Bacmeister/Lindzen Gravity-Wave Drag Parameterization

[8] This gravity-wave drag scheme is an upgraded version of the one discussed by *Summers et al.* [1997] and *Bacmeister et al.* [1998]. It is formulated mathematically in much the same manner as the *Bacmeister* [1993] mountain-wave drag parameterization and models simplified, hydrostatic-wave packets at discrete phase speeds. In philosophy, the approach is similar to the *Lindzen* [1981] parameterization (and thus will be referred hereinafter as the BL parameterization) in that it uses a saturation criterion to determine where waves break. Above the breaking altitude, wave amplitudes remain at the saturated level, or if the saturation criterion no longer holds, unsaturated growth of the wave amplitudes resume, allowing for multiple saturation levels [*Lindzen*, 1985].

[9] Unlike our earlier implementation [*Summers et al.*, 1997; *Bacmeister et al.*, 1998] we now combine both stationary and nonstationary waves into the drag parameterization. We specify each wave's phase speed, amplitude and also a scaling factor with which to multiply the total drag. These choices are summarized in Table 1 and represent the combination used in our two dimensional model results discussed in section 4. We assume that the westward and eastward propagating gravity waves have the same initial vertical displacement amplitudes. The scaling factor is used to tune the zonal winds until they agree with climatology. This tuning factor has analogs in other parameterizations such as the so-called intermittency factor which converts the local momentum flux to a globally averaged value [e.g., *Alexander and Dunkerton*, 1999]. For simplicity, we use the same scaling factor for all 11 individual waves in the model. We also specify the launch altitude; this has been discussed further in section 4.2.

[10] Figure 2 shows the calculated zonal mean flow accelerations, $X$, given by

$$X = \frac{-1}{\rho}\frac{\partial}{\partial z}\left(\rho\overline{u'w'}\right), \tag{1}$$

where $\rho$ is the atmospheric density and $\rho\overline{u'w'}$ is the vertical flux of zonal momentum density, from our gravity wave drag model for both SH summer (January, Figure 2a) and NH summer (July, Figure 2b) CIRA wind fields. A peak eastward acceleration is seen for both cases near 80 km. Since the winds are westward in this altitude region, this

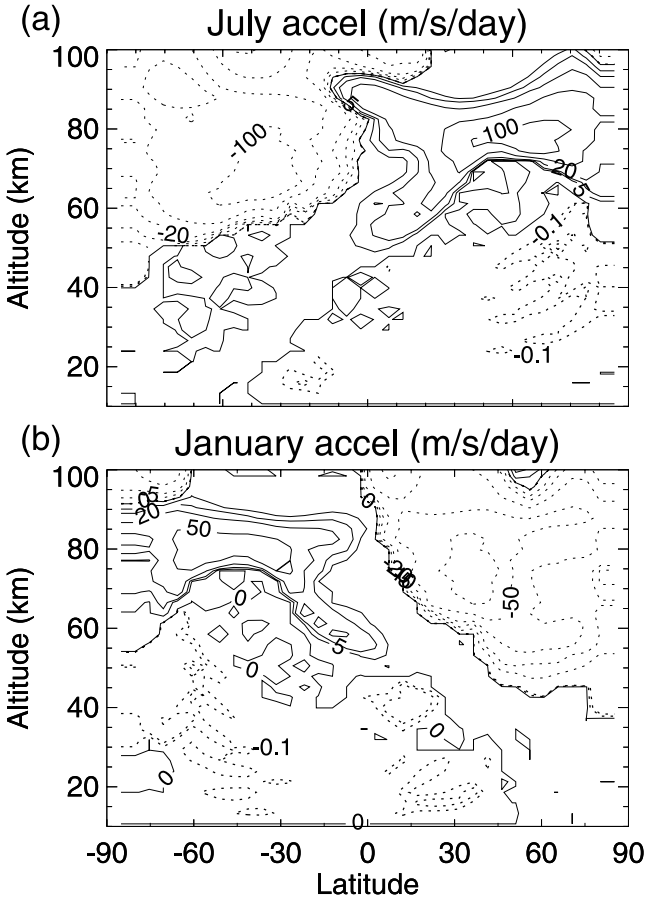


**Figure 2.** Gravity-wave induced accelerations from the Bacmeister/Lindzen (BL) model for July (a) and January (b). The launch amplitudes and phase speeds are given by Table 1; the launch altitude was approximately 13 km (150 hPa). The contours are chosen at pseudologarithmic intervals ±0.1, 0.2, 0.5, 1, 2, 5, 10, 20, 50, 100 m $s^{-1}$ $day^{-1}$. The solid contours are regions of eastward forcing; the dashed contours are regions of westward forcing.

eastward acceleration is effectively a deceleration. Closer inspection of the figure indicates the deceleration is greater in July (peak = 123 m $s^{-1}$ $day^{-1}$ than in January (peak = 100 m $s^{-1}$ $day^{-1}$). As we will discuss, the overall shape of the calculated drag profile and its January/July difference is due to differences in the zonal wind profiles in the upper troposphere and lower stratosphere. Figure 2 also reveals drag contours in the stratosphere which are of opposite sign to those in the upper mesosphere. As discussed by *Alexander and Rosenlof* [1996] and *Alexander and Dunkerton* [1999], this is not drag, but acceleration of the general summertime westward flow. Because our model uses a relatively small set of discrete waves which break at localized altitudes, the calculated drag field is noisy and this noise makes it hard to quantitatively compare the drag profiles in each panel.

[11] To better compare NH and SH summer drag profiles, Figure 3 presents the density-weighted altitude profile $\rho X$, (from (1) above), through the latitude range of the maximum acceleration in Figure 3 (40–50° N for July, 40–50° S for January). Density weighting is helpful here for two reasons. First and most simply, it provides an easy way to visualize the relationship between stratospheric and mesospheric gravity-wave momentum deposition, since the $\rho X$ deviations at all altitudes are more comparable. Second, under the principle of downward control [*Rosenlof and Holton*, 1993; *Haynes et al.*, 1991], $\rho X$ is the integrand in the forcing term for the residual circulation. In Figure 3, we have simply multiplied the profiles in Figure 2 by an assumed $\exp(-z/H)$ term, where H = 7 km is the approximate scale height. The figure shows two regions of momentum deposition: the upper mesosphere, where the July values are greater (in absolute value) than the January values, and the lower stratosphere where the January forcing is greater than July. Thus the stratosphere and mesosphere have opposite N/S summertime asymmetries. *Alexander and Rosenlof* [1996] have suggested that the lower stratospheric difference may account for the observed warmer summers in the SH from 20–50 hPa relative to the NH [see also *Rosenlof and Holton*, 1993]. They theorized that the relatively greater amount of gravity-wave breaking seen in January can drive a slightly stronger downward residual circulation which leads to slightly warmer temperatures. As we will discuss in section 4, our modeling results support this hypothesis.

[12] The sawtooth structure seen in Figure 3 is due to the discrete nature of the assumed gravity-wave phase-speed spectrum. It is instructive to consider the growth and decay of the individual waves in Table 1 in order to gain some insight into which waves are most relevant to producing N/S temperature differences. Figure 4 shows altitude profiles of the vertical displacement amplitudes of each of the 11 waves in Table 1, for the same profiles shown in Figure 3. The increases in amplitude with altitude for each wave is evident. This increase is mainly due to the conservation of wave momentum flux density in an atmosphere of exponentially decreasing density [*Lindzen*, 1981]. In addition, the amplitude growth also depends upon the altitude profile of the instrinsic phase speed, $(c - \bar{u})$, [e.g., *Eckermann*, 1995] and thus the negative phase-speed waves grow more quickly than the positive phase-speed waves in the easterly

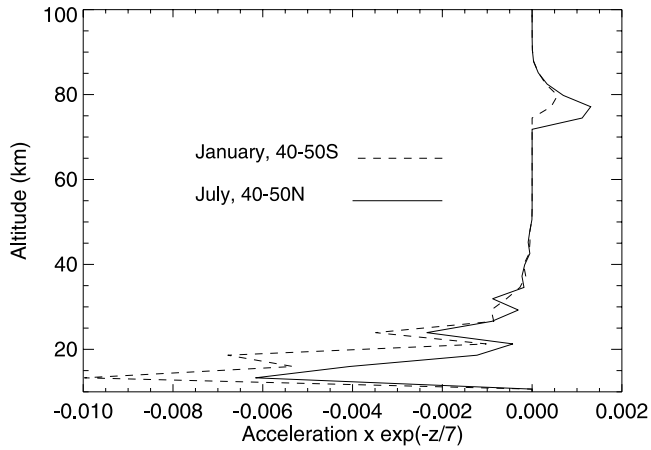


**Figure 3.** Altitude profile of $\rho X$ from gravity-wave breaking obtained by weighting the values in Figure 2 by $exp(-z/7)$ where $z$ is the geometric altitude. The solid line is an average of 40–50N for July; the dashed line is an average of 40–50S for January.

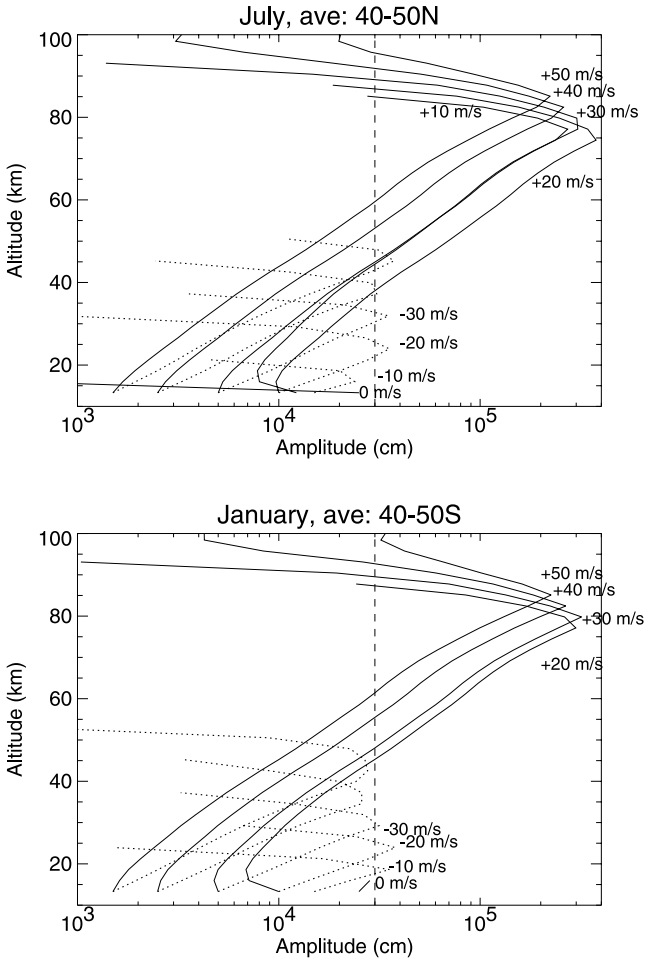


**Figure 4.** Vertical displacement amplitudes of 11 gravity waves in the BL model. The vertical long dashed line is a simple fiducial to aid a better comparison of the lower stratospheric amplitudes.

shear. The sharp turnover in the wave amplitudes represent the onset of saturation, or wave breaking. The saturation altitude and amplitude are different for each phase speed as a result of the dependence of saturation amplitude upon the intrinsic phase speed [*Lindzen*, 1981]. The eastward traveling waves break in the upper mesosphere at which point they have grown to relatively large amplitudes. Note that while the amplitudes of the +30, +40 and +50 m $s^{-1}$ waves are the same for the July and January cases, those of the +10 and +20 m $s^{-1}$ waves are not. Indeed, the +10 m $s^{-1}$ wave is entirely absent for the July case. The reason is that this wave encounters a critical line in the upper troposphere/lower stratosphere (UTLS) in January but not in July. The +20 m $s^{-1}$ wave does not encounter a critical line but it does saturate in the lower stratosphere in January and this limits its amplitude to a small degree relative to the July case. These differences are a direct result of the different UTLS zonal wind profiles between January and July, seen in both the CIRA and NCEP climatologies (Figure 1). The faster tropopause winds in January lead to greater filtering of the +10 and +20 m $s^{-1}$ waves relative to July and less momentum flux is transmitted vertically and available to be manifested as drag in the upper mesosphere in January relative to July.

[13] The westward traveling waves saturate in the lower and middle stratosphere. Here small differences are also seen in the −10, −20, and −30 m $s^{-1}$ waves which break at smaller amplitudes in the NH. This is also due to the weaker winds that the waves encounter in the NH relative to the SH. The amplitudes of the faster waves (−40 and −50 m $s^{-1}$) are more symmetric between NH and SH because these waves do not break until higher in the stratosphere where in the CIRA climatology, the NH and SH summertime wind profiles are more similar. Note that the NCEP climatology suggests greater N/S differences in zonal winds even up into the upper stratosphere.

[14] Figure 4 shows that both the stratospheric and mesospheric differences in gravity-wave drag result from differences in the breaking profiles in the relatively slower (10–30 m $s^{-1}$) phase-speed gravity waves. This is important because it suggests that the existence of N/S differences in gravity-wave drag are linked to the assumption that a significant percentage of the total gravity-wave flux is carried by the 10–30 m $s^{-1}$ waves. This assumption is not well tested as there is great uncertainty in the characteristics of the gravity-wave source spectrum. However, the existence of the relatively well documented stratospheric asymmetry might offer some support for our assumed source spectrum.

### 2.3. Alexander and Dunkerton Gravity-Wave Drag Parameterization

[15] The second gravity-wave drag parameterization we will discuss was presented by *Alexander and Dunkerton* [1999] (hereinafter AD99). This parameterization differs from the BL parameterization in that it is a spectral parameterization based upon linear theory. It uses the breaking criterion of *Lindzen* [1981]; however, while Lindzen-style parameterizations typically assume wave saturation above the breaking level, AD99 simply assume that the momentum fluxes of the waves are deposited totally at the altitude of linear-wave breaking. The model defines a wave source spectrum with fine phase-speed resolution and from the one-to-one correspondence between phase-speed and breaking altitude, the model produces smooth altitude profiles of momentum deposition.

[16] AD99 presented sample calculations of wave-induced mean flow forcing for several gravity source spectra and launch altitudes. Here we show similar results, with emphasis on January/July differences for a narrow ($c_w$ = 20 m $s^{-1}$) and a wide ($c_w$ = 60 m $s^{-1}$) spectrum where $c_w$ is the half width at half maximum of a Gaussian shaped spectrum of momentum flux density as a function of ground-based phase speed. The input flux (.004 Pa) and spectral parameters are similar to those shown Figure 8 ($c_w$ = 20 m $s^{-1}$) and Figure 9 ($c_w$ = 60 m $s^{-1}$) of AD99. The case which comes closest in spectral shape to that used previously in section 2.2 (and in the two-dimensional model) is case 1 ($c_w$ = 20 m $s^{-1}$). Figure 5 shows the acceleration calculated from the AD99 scheme for January and July for this case. The shapes of the drag fields are similar to those obtained from the BL model with some differences in detail. Both models have strong eastward drag in the summer mesosphere and westward drag in the winter

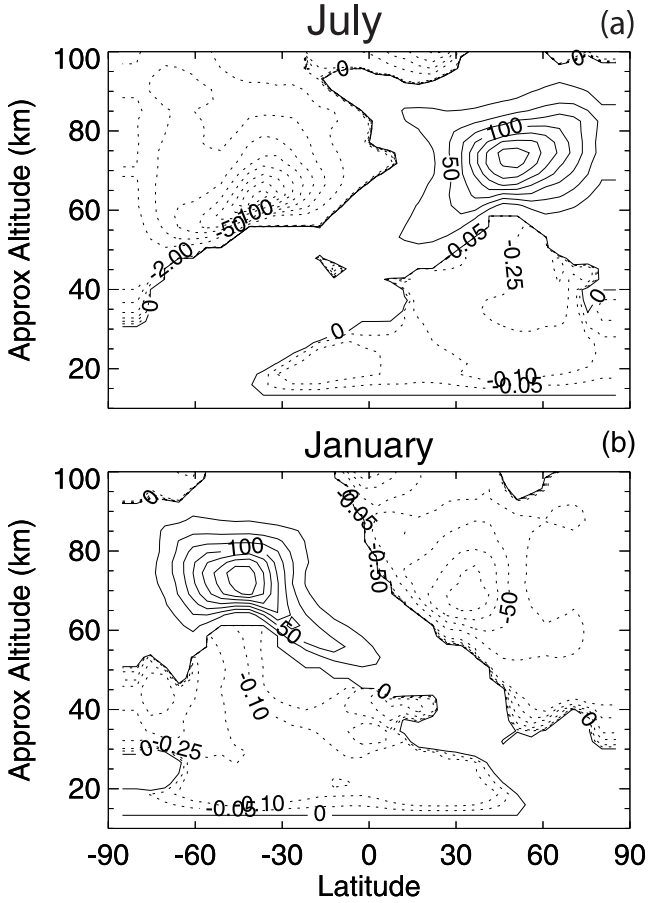


**Figure 5.** Same as Figure 2, but for the AD99 model. The contours are chosen at pseudologarithmic intervals ±0.1, 0.2, 0.5, 1, 2, 5, 10, 20, 50, 100 m $s^{-1}$ $day^{-1}$. The solid contours are regions of eastward forcing; the dashed contours are regions of westward forcing.

mesosphere with the winter drag extending to lower altitudes. The bite-out in the drag field at 40–50° and 65 km, particularly evident in the January results, is due to the existence of the tropospheric jet directly below which filters out the +10 and +20 m $s^{-1}$ waves. Away from this jet core, where the tropospheric winds are weaker, these waves can propagate up to the mesosphere. Since the amplitude distributions assumed for both the BL and AD99 models assume that the slower phase-speed waves are of larger initial amplitude, they tend to break at somewhat lower altitudes (60–70 km). Thus we get a tongue of drag which appears to extend downwards towards lower altitudes and latitudes. The AD99 momentum flux deposition is broader in overall vertical extent than that in Figure 2 and is displaced downward by about 5–10 km relative to the results in Figure 2. These differences likely result from differences in the formulations of the two parameterizations. The AD99 model uses a greater number of phase speeds but also assumes that all the wave momentum flux is deposited at the initial breaking altitude. As far as N/S differences, it is difficult to discern any immediately in Figure 5; however, when we plot altitude profiles of $\rho X$, the density-weighted drag, differences emerge.

[17] Figure 6 shows altitude profiles of $\rho X$, the density-weighted acceleration profiles for a narrow (Figure 6a, $c_w$ = 20 m $s^{-1}$) and a broad (Figure 6b, $c_w$ = 60 m $s^{-1}$) spectrum of waves, for 40–50N (July) and 40–50S (January), in the same format as Figure 3. Figure 6a shows 20–25% more drag in July relative to January in the upper mesosphere and an almost factor of two more forcing in January compared to July in the lowermost stratosphere. Qualitatively this agrees with the results using the BL scheme (Figure 3) although the peak drag in the upper mesosphere occurs lower in altitude (70 km versus 75–78 km) in the AD99 model. AD99 have noted that their parameterization tends to shift the forcing lower down in altitude relative to the more detailed model of *Alexander* [1996]. Again, this is because each spectral component is assumed to deposit all its wave momentum right at the altitude of initial breaking. By contrast, the BL model allows for breaking to continue to higher altitudes. The asymmetry between January and July is smaller with the AD99 model than with the BL model. Since the BL model is used in the actual temperature calculations described in sections 3 and 4, it may be that the dynamically induced temperature differences discussed there are larger than what would be obtained with another gravity model

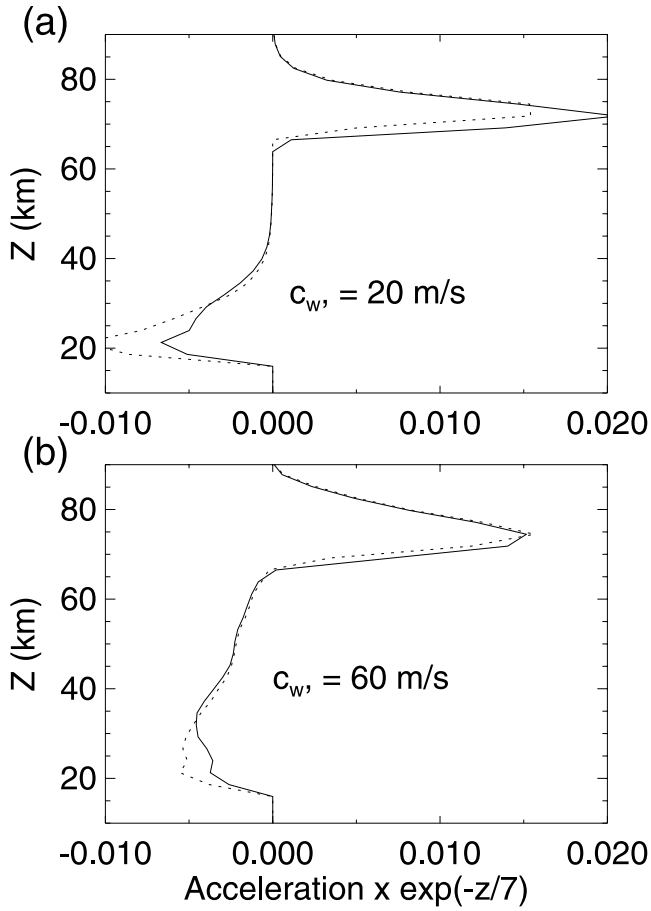


**Figure 6.** Same as Figure 3 but with the AD99 model for two characteristic Gaussian phase-speed distributions (a) $c_w$ = 20 m $s^{-1}$ and (b) $c_w$ = 60 m $s^{-1}$. The assumed horizontal wavelength in both cases is 100 km. The solid lines are for 40–50N, July; the dotted lines are for 40–50S, January.

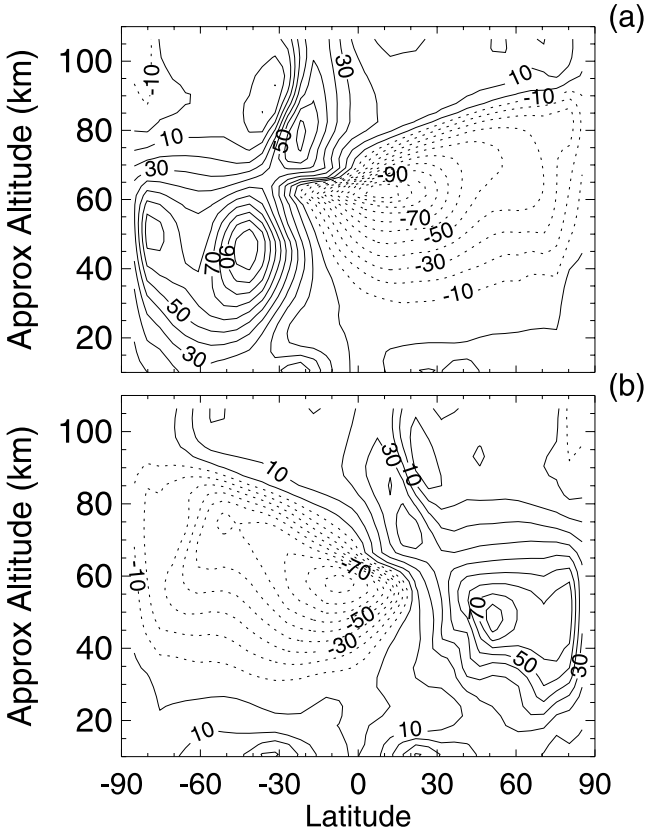


**Figure 7.** Model zonal wind fields for July (a) and January (b). The solid contours indicate regions of eastward winds; the dashed contours indicate regions of westward winds. The approximate altitude scale is derived from the pressure grid in the model according to z = −7*ln(p/1000).

such as the AD99 model. In Figure 6b, with a broader spectrum, the mesospheric asymmetry disappears and the stratospheric asymmetry is sharply reduced. Thus as with the BL model, both the upper and lower altitude differences are due to the relatively slower ($|c| < 30$ m s$^{-1}$) waves.

[18] In summary, both the BL and AD99 gravity-wave drag parameterizations suggest the existence of N/S asymmetries in gravity-wave drag in the summer polar mesosphere. Further they both suggest that in the stratosphere greater westward forcing occurs in the SH while in the mesosphere, stronger eastward forcing occurs in the NH. In both cases, these N/S asymmetries are linked to the greater eastward winds (westerlies) in the SH troposphere and lower stratosphere. These faster westerlies cause both greater filtering of positive (eastward) phase-speed waves and stronger breaking of negative (westward) phase-speed waves. This effect is most pronounced for waves with phase speeds on the order of the wind speed, $|c| < 30$ m s$^{-1}$. Faster waves are less affected and exhibit the most symmetric drag between the NH and SH (Figure 6b).

## 3. Two-Dimensional Chemical Transport Modeling

### 3.1. Summary of Model Upgrades

[19] The basic formulation of the NRL two dimensional chemical transport model has been described previously [*Summers et al.*, 1997; *Siskind et al.*, 1997; *Bacmeister et al.*, 1998; *Siskind et al.*, 1998; *Siskind*, 2000]. Briefly, the dynamical component of the model is based upon the Transformed-Eulerian-Mean (TEM) formulation [*Garcia and Solomon*, 1983] which solves for the evolution of zonally averaged angular momentum ($\overline{M}$) and potential temperature ($\overline{\Theta}$). The calculated $\overline{M}$ and $\overline{\Theta}$ fields are used to derive an elliptic equation for the stream function $\Psi$ from which the residual meridional ($v^*$) and vertical ($w^*$) wind fields are obtained. The model extends from the ground to $p = 2x10^{-4}$ hPa (approximately 100–108 km). Since the work of *Siskind* [2000] we have improved the model in several ways, the most important of which is in the specification of the momentum forcing due to dissipating gravity waves. As was discussed in section 2.2, we now combine previously separate parameterizations for stationary and nonstationary waves. Previously, the stationary (i.e., mountain) waves were crudely approximated by a prescribed cubic law drag term with an altitude dependent friction coefficient. In order to simulate the observed difference between Northern and Southern winters, we assumed that the mountain waves broke at a higher altitude in the SH. This led to less drag in the stratosphere, but more in the mesosphere, and yielded a N-S difference in the zonal wind and in the winter descent which was in good qualitative agreement with observations [*Siskind*, 2000].

[20] For summer conditions, the above approach is inappropriate because the existence of a zero wind line in the lower stratosphere should preclude the propagation of mountain waves into the middle atmosphere. We now use the extended BL gravity wave scheme described in section 2.2 to calculate the drag. The gravity-wave parameters are the same as in Table 1, except that we assume a latitudinal variation in the launch amplitudes of $(1 + |\sin(2\theta)|)/2.0$ where $\theta$ is the latitude. Our planetary-wave forcing is the same as in previous publications [*Siskind*, 2000], in that we assume a geopotential height displacement that is twice as large in the NH as in the SH to reflect the greater planetary-wave activity in the north. Because the model gives a better representation of the drag on the zonal flow, we have been able to completely remove Rayleigh friction from our stratospheric calculation (previously we used a 100 day damping time scale with an undamped regime only in the tropics; this is retained in the mesosphere). Other minor improvements include the use of MSIS atomic oxygen at the top boundary and the use of NCEP winds below 6 km in the planetary-wave model.

[21] In the calculations described below, the dynamical and chemical calculations were fully coupled. Thus we use the model-calculated ozone to drive the radiative calculation and the calculated O, OH, H, $O_3$ and $HO_2$ fields to calculate chemical heating effects in the mesosphere [*Mlynczak and Solomon*, 1993]. We also have updated the rate coefficient for the $O + CO_2$ reaction (used in our mesospheric radiative code [*Zhu et al.*, 1992]) to $3 \times 10^{-12}$ cm$^3$ s$^{-1}$ as suggested by *Lopez-Puertas et al.* [1998]. Sensitivity studies that we have performed suggest a 15K difference in the calculated temperature at and above 100 km when we let this rate coefficient vary between the value of $5.5 \times 10^{-12}$ cm$^3$ s$^{-1}$ suggested by *Wintersteiner et al.* [1992] and the value of $1.3 \times 10^{-12}$ suggested by *Pollack et al.* [1993]; however, this difference is <5K below 95 km. In this coupled simulation we found that our age-of-air maximized at ~4 years in the

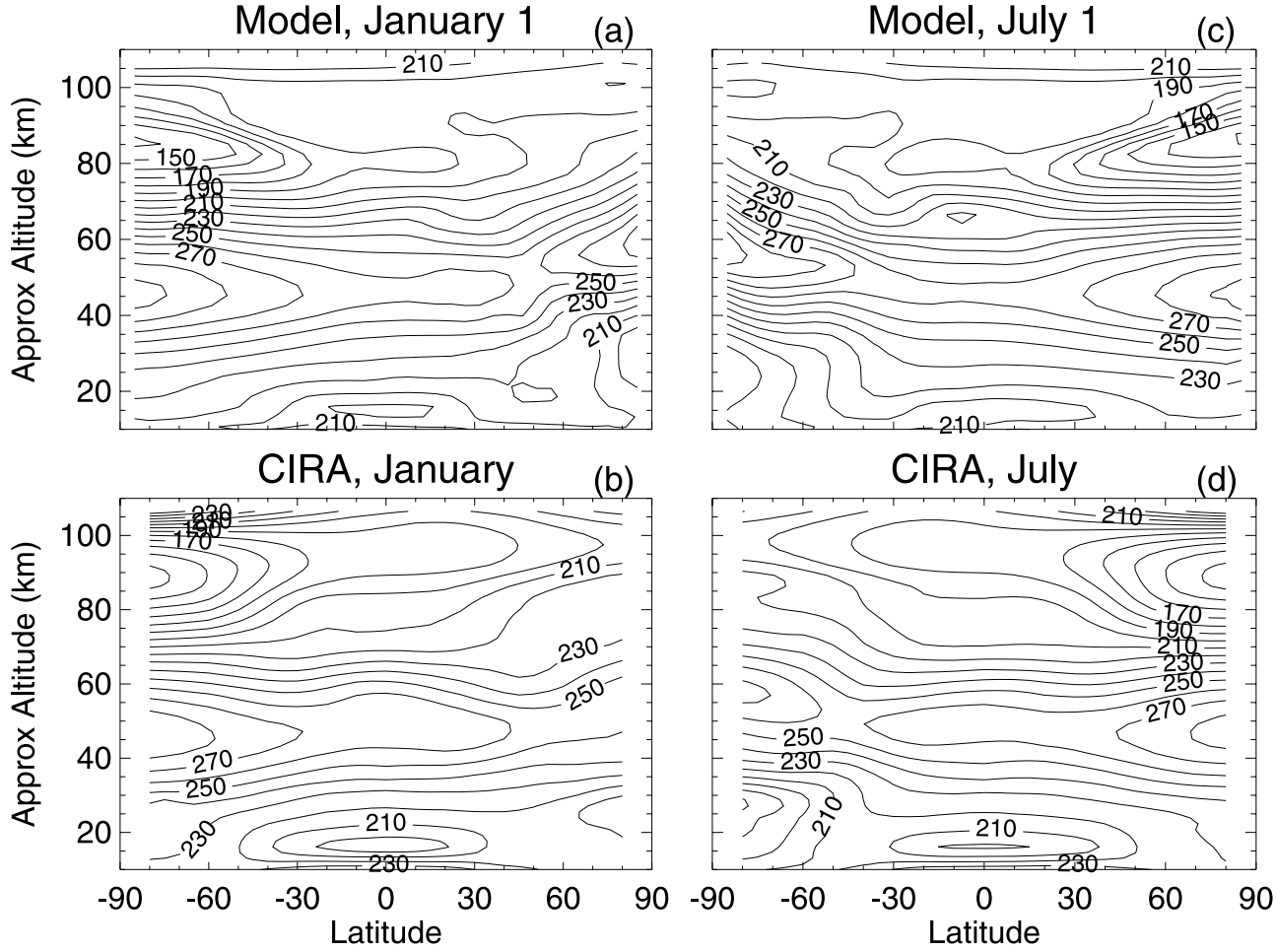


**Figure 8.** Model temperature fields for January and July ((a) and (c)) and CIRA climatology ((b) and (d)).

lower mesosphere which is probably too young [*Hall et al.*, 1999]. In order to increase the age to values closer to observations (>5 years at 50 km), we divided our tropical tropospheric latent heat values [see *Bacmeister et al.*, 1998] by a factor of 2. Finally, and most importantly for N-S differences, we explicitly consider the effects of orbital eccentricity in the radiative heating calculation.

### 3.2. Model Results

[22] Figures 7–10 present the relevant model diagnostics pertinent to our discussion of north/south differences. The model zonal wind fields in Figure 7 can be compared with the climatologies in Figure 1. Also instructive are the mean zonal wind fields presented by *Lieberman et al.* [2000] for 65–105 km for early 1994. As in earlier versions of the model, the winds are in generally good agreement with the data; however, in this case we achieve this agreement with fewer a priori assumptions about the drag profiles. Specifically, the faster upper stratospheric winter westerlies in July (SH) relative to January (NH), which are an obvious feature of the NCEP and CIRA climatologies, originate solely from the weaker planetary-wave forcing assumed in the model. The faster SH stratospheric winds mean that mountain waves saturate at a higher altitude in the SH than in the NH, consistent with the discussion of *Garcia et al.* [1992]. The magnitudes of the winter westerlies are approximately correct, although the altitude profile in the subtropical lower mesosphere differs from the CIRA climatology. In summer, the model also simulates the approximate magnitude of the tropospheric westerlies and their N/S difference. The faster tropopause jet at 30S in January relative to 30N in July also results from the stronger planetary-wave drag in the NH. Note that neither the model simulation nor the CIRA wind climatology realistically represent tropical dynamics. For more recent results on tropical dynamics, see *McCormack and Siskind* [2002].

[23] The model results exhibit several disagreements with the NCEP and CIRA climatologies which are worth mentioning. One problem is that the westward shear in the summertime lower stratosphere is too weak. *Alexander and Rosenlof* [1996] suggest that the inability of a model to damp out the tropospheric summer westerlies may reflect insufficient gravity-wave drag in the lower stratosphere. Second, in the upper mesosphere, our winds are generally too weak. The winter westerly jet is damped out too quickly above 60 km in our model. This may be related to our overly warm winter stratopause (discussed below) and suggests perhaps too much drag. Third, the removal of Rayleigh friction resulted in very fast low latitude summer easterlies. Finally, in summer, we do not simulate the strong westerly jet in the lower thermosphere which is evident in the CIRA climatology and in the *Lieberman et al.* [2000] data. This

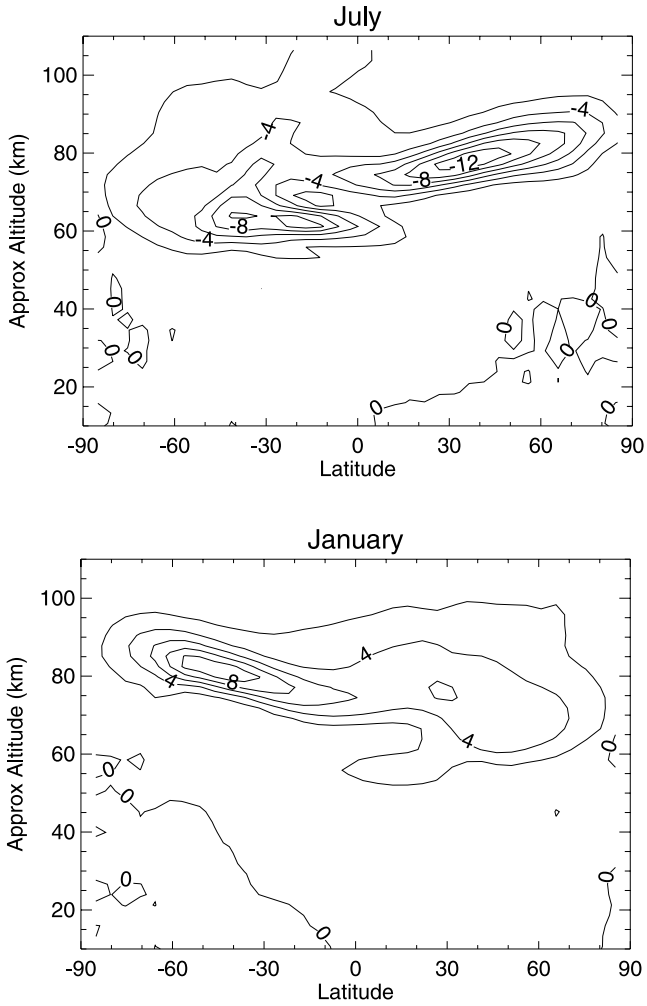


**Figure 9.** Model $v^*$ for January and July. The contours are labeled in m $s^{-1}$.

may be due to insufficient flux of fast (>50 m $s^{-1}$) phase-speed gravity waves or a consequence of the proximity of our top boundary to the core of this jet. We are likely not capturing the effects of gravity waves which might be breaking above 105 km and contributing to this jet.

[24] We should stress that, with one exception, we assume seasonally invariant gravity-wave and planetary-wave amplitudes. This is undoubtedly an oversimplification; however, there are enough uncertainties in the variation of these wave forcings that trying to tune the model further would be unwarranted. A persistent problem with our model which did not improve in the current version is that the breakdown of the winter polar vortex associated with the final spring warming occurs much too late, typically December in the SH and April in the NH [e.g., *Siskind et al.*, 1997]. To "jump start" the spring warming, we doubled the amplitude of the planetary-wave forcing on October 15 in the SH and March 15 in the NH for about a 1–2 month period.

[25] Figure 8 shows the calculated January and July temperature fields and compares them to CIRA. The cold summer mesopause in the model is clearly shown with temperatures that now fall below 140K in the SH and below 130K in the NH. It is also evident that the NH summer mesopause is colder than the SH. This is mainly, but not entirely, due to the stronger residual circulation in July than in January and will be explored further below. The model shows a warm winter stratopause with a peak temperature of approximately 280 K, warmer than CIRA, but well within the monthly mean values observed in numerous individual winters [e.g., *Lubken and von Zahn*, 1991; *Gerrard et al.*, 2000]. The model accurately captures the winter N/S differences with a warmer stratopause in the SH due to greater SH mesospheric descent and a warmer lower and middle stratosphere in the NH, due to greater NH planetary wave activity. Finally, one persistent problem area is our low and midlatitude latitude mesopause temperatures which, at 180–190 K, may be in good agreement with CIRA, but remain systematically too cold compared with newer data sets such as *Yu and She* [1995], *Clancy et al.* [1994] and *States and Gardner* [2000] [see also *Siskind et al.*, 1997, Figure 8]. This problem may not be unique to our model; for example *Akmaev* [2001] recently presented results from a 3D model which are systematically colder than CIRA by up to 10K and thus probably 20–30K colder than the actual atmosphere. In our case, our overall gravity-wave momentum deposition may be too large right at 80 km. The drag fields derived by *Lieberman et al.* [2000] are spread over a wider range of altitudes than what we have shown in Figures 2 and 5.

[26] Figure 9 shows the transformed Eulerian meridional wind, $v^*$, for January and July. The stronger residual circulation in July is evident and due to the larger gravity-wave drag relative to January as illustrated by our CIRA

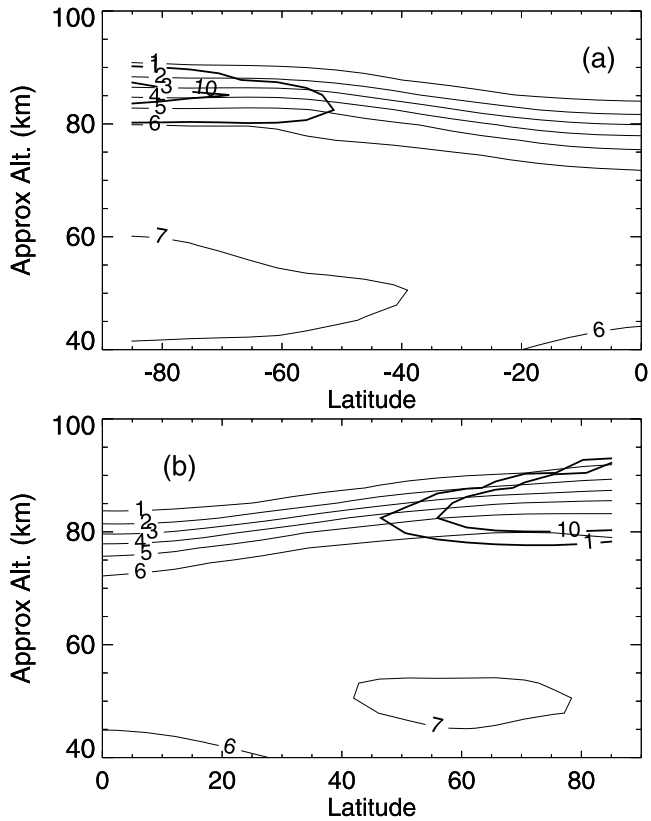


**Figure 10.** Summer $H_2O$ (units of ppmv) from the 2D model for January (a) and July (b) with S = 1 and S = 10 contours overlain with thick black lines.

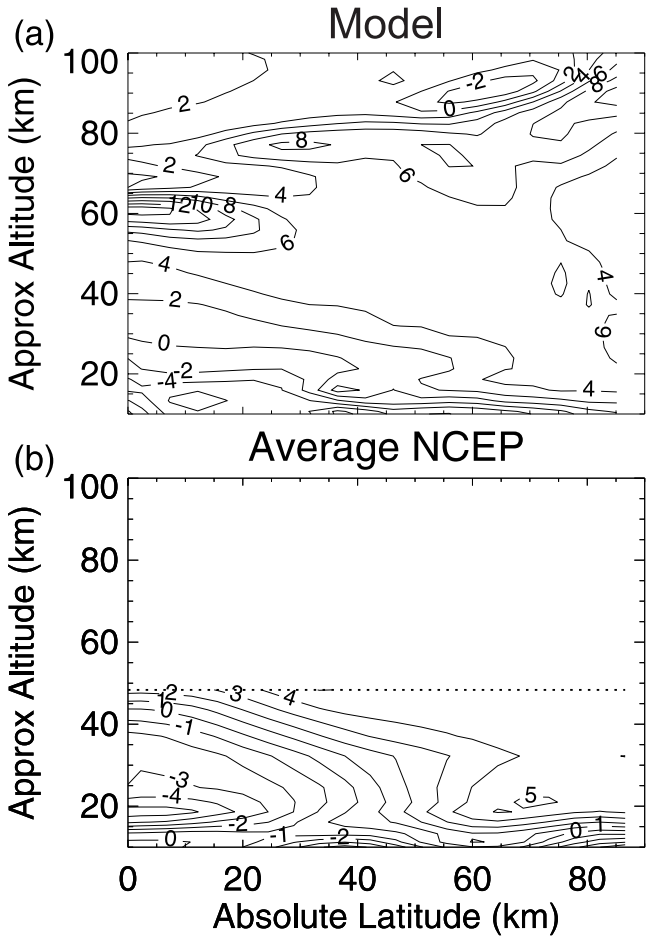


**Figure 11.** (a) Model N-S temperature difference (January (SH)–July (NH)), compared with (b) NCEP average. The horizontal dotted line in (b) indicates the top altitude of the NCEP analysis.

analysis in section 2. Compared with the $v^*$ inferred by *Lieberman et al.* [2000] from High Resolution Doppler Interferometer (HRDI) data, our results are in general agreement in magnitude, but with some differences in morphology. *Lieberman et al.* [2000] find a peak $v^*$ above 100 km which we do not, probably for the same reason we underestimate the zonal winds, i.e., the proximity of our top boundary. They also see a secondary maximum in $v^*$ at 80–90 km in January and near 70 km in July which has not been reported previously and is not present in our model. Like our model, *Lieberman et al.* [2000] find larger $v^*$ below 100 km in July compared with January.

[27] Finally, given that our model predicts a colder mesopause in July relative to January, it is of interest to see what this might mean for PMC formation. A detailed microphysical calculation is well beyond the scope of this paper; rather, we simply show in Figure 10 the calculated water vapor fields for July and January. The calculated $H_2O$ mixing ratios are little changed from our previous publications and there is little N-S difference. However, overlaid in Figure 10 are the $S = 1$ and $S = 10$ contours defined as $S = p_{H2O}/p_{sat}$ where $p_{H2O}$ is the water vapor pressure and $p_{sat}$ is the saturation vapor pressure. It is clear that much more extensive supersaturation is implied in the NH due to the colder temperatures and the strong dependence of relative humidity upon temperature. Of course, *Summers et al.* [2001] recently have shown that observations of the water vapor altitude profile in the summer polar latitude region differ substantially from that suggested by Figure 10. This is likely due to condensation/sublimation effects associated with the formation of PMCs, an effect which is poorly understood and is not currently addressed by our model. However, as *Summers et al.* [2001] note, the ultimate source of $H_2O$ to the mesopause region is still believed to be from upwelling and as long as that is the case, the contours in Figure 10 are useful guides to N-S differences in that source. If the N/S temperature asymmetry is anything like that suggested by our model, our results would imply that PMC/NLC/PMSE formation should be favored in the NH relative to the SH.

## 4. Discussion

### 4.1. Radiative Versus Dynamical Effects

[28] We have shown in section 3 that our two-dimensional model predicts a colder and more humid NH summer

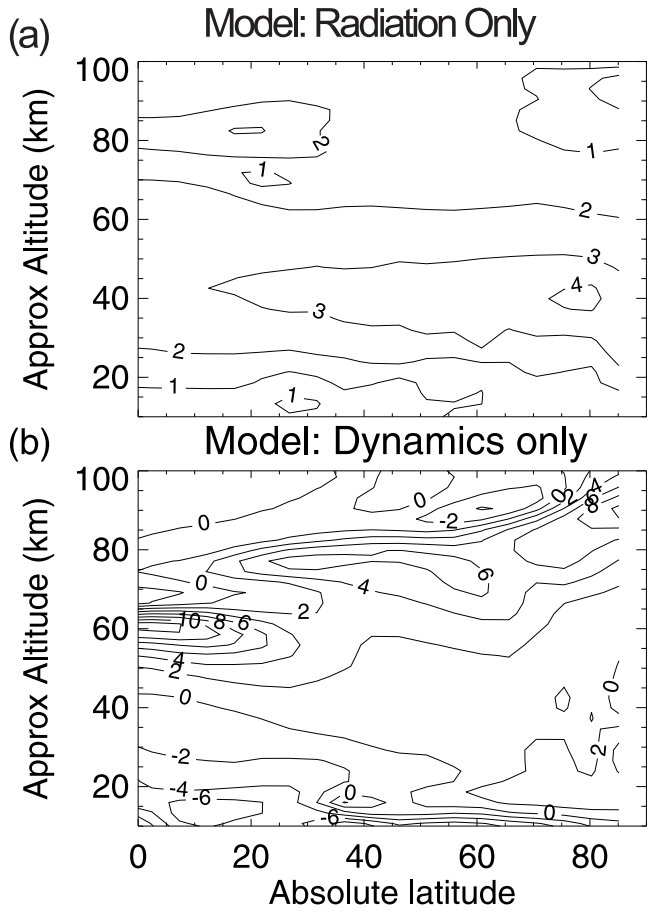


**Figure 12.** Decomposed model N-S temperature differences. The top panel (a) is a model calculation with hemispherically symmetric dynamical inputs (planetary wave forcing, tropospheric temperatures), but assumes an eccentric orbit in the radiative calculation. The bottom panel (b) assumes a circular orbit, but with N-S asymmetries in the dynamical forcing.

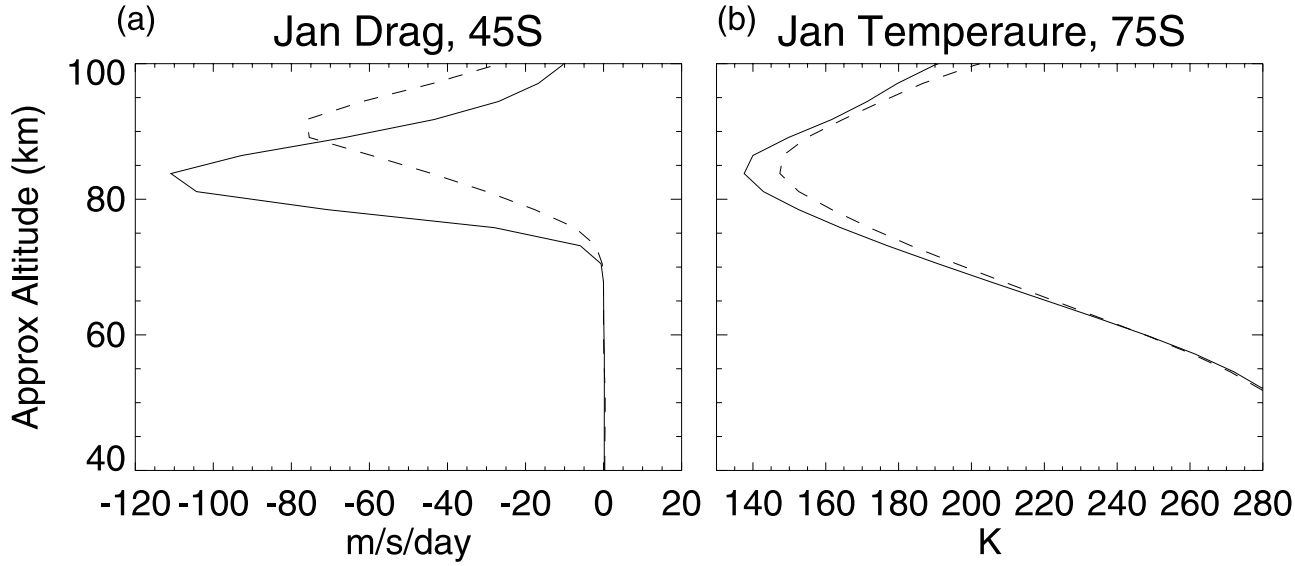


**Figure 13.** Effect of different launch altitudes for the gravity waves on (a) the midlatitude drag profile and (b) polar summer temperatures in the 2D dynamical/chemical model. The solid line is the original calculation which assumes a launch altitude of 16 km. The dashed line assumes a launch altitude of 9 km.

mesopause relative to the SH and argued that most, but not all, of this is due to greater dynamical forcing in July relative to January. One factor which also must be considered is Earth's orbital eccentricity. Since Earth is 3.4% closer to the Sun in January relative to July, the radiative forcing is about 7% greater during Southern summer. This has consequences throughout the middle atmosphere as will show.

[29] Figure 11 presents the differences between SH and NH summer temperature (January–July) in the model for both the stratosphere and mesosphere and compares them with observations of the stratosphere from an average of NCEP data. The model shows a broad region where the SH is warmer than the NH by more than 3K from the lower stratosphere to the upper mesosphere. The temperature difference shows a primary peak in the 80 km region of over 6–8K and a secondary peak of over 4–6K in the high latitude lowermost stratosphere (a third region in the tropical lower mesosphere may be connected to a weak semi-annual oscillation (SAO) and is beyond the scope of this discussion). While the upper mesospheric peak lies outside the domain of the NCEP data, the stratospheric peak is in good qualitative agreement with the 4–5K maximum temperature difference seen in the data poleward of 60°. The NCEP data do not show the 6–8K peak seen in the UKMO data presented by *Rosenlof* [1996]; however, as she shows, the actual morphology of the N/S difference is not exactly the same among the various analyses and observations.

[30] The roles of radiation and dynamics in producing the model N/S difference are shown in Figure 12. Figure 12a presents a model calculation where all the dynamical forcing (planetary waves, surface temperature boundary conditions) was completely symmetrized between the NH and SH and only the radiative effects of an eccentric orbit were considered. It shows a broad region of warmth centered at 40 km where the peak is 4K. This altitude distribution is directly related to the peak ozone heating. Note that nonzero temperature differences extend above 80 km and below 20 km. Figure 12b is from a calculation where the dynamical asymmetries were retained, but Earth's orbit was assumed to be completely circular. Here the effect yields a much more complicated pattern that is more similar to the complete solution seen in Figure 11a. We see an 80 km peak of >6K which falls to 0–2K in the 40–60 km region and then a small increase below 20 km at high latitudes. The 80 km peak results from the weaker mean meridional circulation in January relative to July and is traceable ultimately to the 25–30% less gravity-wave drag seen in January and dis-

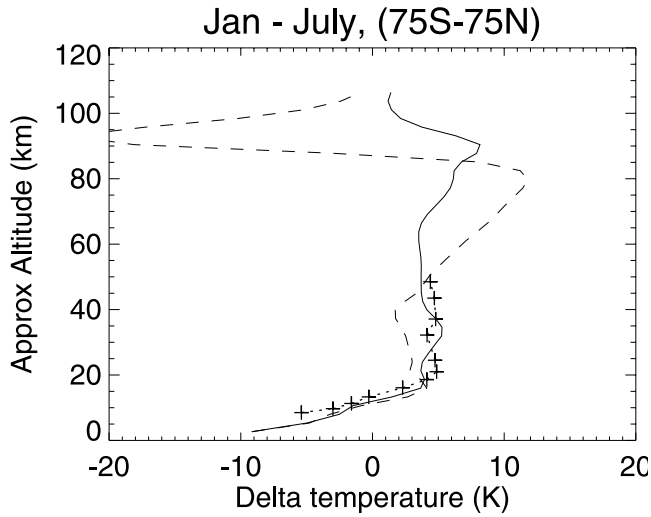


**Figure 14.** Effect of gravity-wave launching height on calculated N/S temperatures differences. The solid lines are the model with gravity waves launched at 16 km; this profile is a vertical slice through Figure 11a at 75°. The dashed line is for the calculation with a 9 km launch altitude. The stars are the NCEP summer temperature difference (SH-NH, dotted line with stars) for 75°, taken from Figure 11b.

cussed in section 2. Conversely, the high latitude lower stratospheric warmth is connected to a small region of net downwelling in the SH as opposed to near zero $w^*$ in the NH in this altitude region and is also traceable ultimately to the differing gravity-wave forcing discussed in section 2. Thus while the relative role of direct radiative effects in producing N/S temperature differences even down to 20 km is perhaps greater than anticipated by *Rosenlof* [1996], our results do in general support her suggestion that dynamical asymmetries play a role.

### 4.2. Effects of Gravity-Wave Launch Altitude

[31] One uncertainty in our gravity-wave drag parameterization (and most others) is the launch altitude. Many models [e.g., *Norton and Thuburn*, 1999; *Akmaev*, 2001] assume that the gravity waves are launched at around 100 hPa. However, *Alexander and Dunkerton* [1999] explored different launch altitudes between the ground and the tropopause and *Manzini and McFarlane* [1998] used a 3D model to focus on the difference between two simulations, one in which the gravity waves were launched at 110 hPa and the other with the waves launched at the ground.

[32] Figure 13 shows the effects of launching gravity waves in the 2D model from 9 km as compared with launching from 16 km. The same spectrum is used in both simulations. By launching at 9 km, we expose a greater fraction of the eastward traveling waves to possible critical lines in the tropospheric westerly jet. Thus the momentum deposition in the mesosphere is reduced as seen in Figure 13a and discussed by *Manzini and McFarlane* [1998]. The reduction in midlatitude drag weakens the global residual circulation and thus increases the polar summer mesopause temperature by about 10K. This second result differs from *Manzini and McFarlane* [1998]; however, much of the difference is above 80 km which is above the top boundary of their model.

[33] Figure 14 shows the Jan–July difference at 75° latitude for the two model runs (9 km launch and 16 km launch) as a function of height along with the NCEP data at ±75° from Figure 11b. The hemispheric difference in the new model run (9 km launch) shows a different morphology than in the old (16 km launch). The general SH warmth remains evident, but between 15 and 40 km it is less than before (and less than the data), between 45 and 80 km it is greater than before and then above 85 km (the mesopause) there is a region where the SH is sharply colder than the NH. This cold layer occurs because in the SH with the 9 km launching altitude, the gravity-wave drag is displaced much more noticeably to higher altitudes. Thus above 90 km, there is greater drag in the January SH than in the July NH; this leads to colder temperatures. A hint of this SH cold layer can be seen in the −2K contour in Figure 12b which shows up at 60° and 90–95 km.

[34] While the agreement with the NCEP data is somewhat poorer for the 9 km launch case, this result is useful for two reasons. First dynamically driven N-S differences are a persistent feature of our simulations. Second, if the atmospheric asymmetry exhibits the sort of layering indicated Figure 14, it might at least partially explain the apparent null result of *Lubken et al.* [1999]. With a quoted minimum vertical resolution of 8 km at 85 km, their falling sphere technique might not have the altitude resolution to separate out a narrow layer of SH warmth from NH warmth. This highlights the need for more high vertical resolution polar mesopause temperature data.

## 5. Conclusions

[35] The most robust result of our calculations is that the SH summertime middle atmosphere should be warmer than the NH, at least up to the mesopause. The robustness of this result stems from its link to other better documented atmospheric phenomena such as the winds and temperatures in the lower stratosphere. Our calculations generally support the suggestions of *Rosenlof* [1996] and *Alexander and Rosenlof* [1996] that small-scale dynamical differences between the NH and SH are important for understanding the warmer SH stratospheric summer. However, direct radiative effects due to Earth's orbital eccentricity are not insignificant between 20 and 65 km. Furthermore, our results suggest the possibility that the lower stratospheric SH warmth relative to the NH may be linked to a similar warmth in the upper mesosphere. This link might offer some support for our (admittedly simplistic) assumptions about the nature of the gravity-wave spectrum entering the middle atmosphere and the way it dissipates. For example we assumed a source strength which was the same in both the NH and SH. The fact that the two-dimensional model appears to capture the stratospheric temperature asymmetry may provide some justification for this assumption.

[36] Our results generally support those studies [e.g., *Vincent*, 1994] which suggest a stronger mesospheric residual circulation in July relative to January. They would, at first glance, appear to be inconsistent with the *Lubken et al.* [1999] falling sphere temperature data; however, the narrowness of the upper mesospheric SH warm layer may be difficult for their technique to resolve. Our findings are important because of their implications for observables such as PMCs/NLCs and PMSE. If the SH mesopause is truly 3–7K warmer than the NH, all these phenomena should be weaker or less frequent in the SH. This may indeed be the case for PMSE [*Woodman et al.*, 1999]; however, if that is so, it is surprising that such a difference has not been reported for the visible clouds [*Carbary et al.*, 1999; *Chu et al.*, 2001]. There are additional PMC data sets currently being analyzed (e.g., the Student Nitric Oxide Explorer, SNOE) [*Bailey et al.*, 2001] and planned (the Aeronomy of Ice in the Mesosphere, AIM) which should shed new light on this important question.

[37] Finally, although we have not studied the sensitivity of this result to hemispheric variability in gravity-wave sources, it would be interesting if the asymmetry proved sensitive to intraseasonal or interannual variability in the source production and jet stream winds in each hemisphere. There has been recent speculation on a link between interannual variability in sea surface temperatures and tropospheric weather patterns and conditions at the summer mesopause [*Sassi et al.*, 2001]; the mechanism discussed here, wave filtering by the varying zonal flow in the summertime upper troposphere and lower stratosphere, may be relevant to better understand how such a proposed coupling could occur.

[38] **Acknowledgments.** Funding for this work at the Naval Research Laboratory has come in part from the Office of Naval Research and the NASA Geospace Science Program and at Colorado Research Associates, from National Science Foundation grant ATM-9907501. We thank Bill Randel for his assistance in making the NCEP data available to us and Mike Stevens for discussions on water vapor condensation.

## References

Akmaev, R. A., Simulation of large-scale dynamics in the mesosphere and lower thermosphere with the Doppler-spread parameterization of gravity waves, 1, Implementation and zonal mean climatologies, *J. Geophys. Res.*, *106*, 1193–1204, 2001.

Alexander, M. J., A simulated spectrum of convectively generated gravity waves: Propagation from the tropopause to the mesopause and effects on the middle atmosphere, *J. Geophys. Res.*, *101*, 1571–1588, 1996.

Alexander, M. J., and T. J. Dunkerton, A spectral parameterziation of mean-flow forcing due to breaking gravity waves, *J. Atmos. Sci.*, *56*, 4167–4182, 1999.

Alexander, M. J., and K. H. Rosenlof, Nonstationary gravity wave forcing of the stratospheric zonal mean wind, *J. Geophys. Res.*, *101*, 23,465–23,474, 1996.

Bacmeister, J. T., Mountain-wave drag in the stratosphere and mesosphere inferred from observed winds and a simple mountain-wave parameterization scheme, *J. Atmos. Sci.*, *50*, 377–399, 1993.

Bacmeister, J. T., D. E. Siskind, M. E. Summers, and S. D. Eckermann, Age of air in a zonally averaged two-dimensional model, *J. Geophys. Res.*, *103*, 11,263–11,288, 1998.

Bailey, S. M., G. E. Thomas, and A. W. Merkel, The climatology of polar mesospheric clouds from the Student Nitric Oxide Explorer, *EOS Trans. AGU*, *82*(47), Spring Meet. Suppl., abstract SA31B-05, 2001.

Carbary, J. F., et al., Altitudes of polar mesospheric clouds observed by a middle ultraviolet imager, *J. Geophys. Res.*, *104*, 10,089–10,100, 1999.

Chu, X., C. S. Gardner, and G. Papen, Lidar observations of polar mesospheric clouds at South Pole: Seasonal variations, *Geophys. Res. Lett.*, *28*, 1203–1206, 2001.

Clancy, R. T., D. W. Rusch, and M. T. Callan, Temperature minima in the average thermal structure of the middle mesosphere (70–80 km) from analysis of 40- to 92-km SME global temperature profiles, *J. Geophys. Res.*, *99*, 19,001–19,020, 1994.

Dowdy, A., R. A. Vincent, K. Igarashi, Y. Murayama, and D. J. Murphy, A comparison of mean winds and gravity wave activity in the northern and southern polar MLT, *Geophys. Res. Lett.*, *28*, 1475–1478, 2001.

Eckermann, S. D., Effect of background winds on vertical wave number spectra of atmospheric gravity waves, *J. Geophys. Res.*, *100*, 14,097–14,112, 1995.

Fleming, E. L., S. Chandra, J. J. Barnett, and M. Corney, Zonal mean temperature, pressure, zonal wind, and geopotential height as functions of latitude, COSPAR International Reference Atmosphere: 1986, II, Middle atmosphere models, *Adv. Space Res.*, *10*(12), 11–59, 1990.

Garcia, R. R., F. Stordal, S. Solomon, and J. T. Kiehl, A new numerical model of the middle atmosphere, 1, Dynamics and transport of tropospheric source gases, *J. Geophys. Res.*, *97*, 12,967–12,991, 1992.

Gerrard, A. J., T. J. Kane, and J. Thayer, Year-round temperature and wave measurements of the Arctic middle atmosphere for 1995–1998, in *Atmospheric Science Across the Stratopause*, *Geophys. Monogr. Ser.*, vol. 123, edited by D. E. Siskind et al., pp. 213–219, 2000.

Hall, T. M., D. W. WAugh, K. A. Boering, and R. A. Plumb, Evaluation of transport in stratospheric models, *J. Geophys. Res.*, *104*, 18,815–18,841, 1999.

Haynes, P. H., C. J. Marks, M. E. McIntyre, T. G. Shepherd, and K. P. Shine, On the "downward control" of extratropical diabatic circulations by eddy-induced mean zonal forces, *J. Atmos. Sci.*, *48*, 651–678, 1991.

Huaman, M. M., and B. B. Balsley, Differences in near-mesopause summer winds, temperatures, and water vapor at northern and southern latitudes as possible causal factors in inter-hemispheric PMSE differences, *Geophys. Res. Lett.*, *26*, 1529–1532, 1999.

Lieberman, R. S., et al., Comparison of mesospheric and lower thermospheric residual wind with High-Resolution Doppler Imager, medium frequency, and meteor radar winds, *J. Geophys. Res.*, *105*, 27,023–27,035, 2000.

Lindzen, R. S., Turbulence and stress owing to gravity wave and tidal breakdown, *J. Geophys. Res.*, *86*, 9707–9714, 1981.

Lindzen, R. S., Multiple gravity-wave breaking levels, *J. Atmos. Sci.*, *42*, 301–305, 1985.

Lopez-Puertas, M., G. Zaragoza, M. A. Lopez-Valverde, and F. W. Taylor, Nonlocal thermodynamic equilibrium (LTE) atmospheric limb emission at 4.6 um, 1, An update of the CO2 non-LTE raidative transfer model, *J. Geophys. Res.*, *103*, 8499–8514, 1998.

Lubken, F.-J., and U. von Zahn, Thermal structure of the mesopause region at polar latitudes, *J. Geophys. Res.*, *96*, 20,841–20,856, 1991.

Lubken, F.-J., M. J. Jarvis, and G. O. L. Jones, First in situ temperature measurements at the Antarctic summer mesopause, *Geophys. Res. Lett.*, *26*, 3581–3584, 1999.

Manzini, E., and N. A. McFarlane, The effect of varying the source spectrum of a gravity wave parameterization in a middle atmosphere general circulation model, *J. Geophys. Res.*, *103*, 31,523–31,539, 1998.

McCormack, J. P., and D. E. Siskind, Simulations of the quasi-biennial oscillation and its effect on stratospheric H2O, CH4, and age of air with an interactive two-dimensional model, *J. Geophys. Res.*, *107*, 4625, doi:10.1029/2002JD002141, 2002.

Mlynczak, M. G., and S. Solomon, A detailed evaluation of the heating efficiency in the middle atmosphere, *J. Geophys. Res.*, *98*, 10,517–10,542, 1993.

Norton, W. A., and J. Thuburn, Sensitivity of mesospheric mean flow, planetary waves, and tides to strength of gravity wave drag, *J. Geophys. Res.*, *104*, 30,897–30,911, 1999.

Pollock, D. S., G. B. I. Scott, and L. F. Phillips, Rate constant for quenching of CO2(010) by atomic oxygen, *Geophys. Res. Lett.*, *20*, 727–729, 1993.

Randel, W. J., Global atmospheric circulation statistics 1000-1 mb, *NCAR Tech. Note 366*, Natl. Cent. for Atmos. Res., Boulder, Colo., 1992.

Rosenlof, K. H., Summer hemisphere differences in temperature and transport in the lower stratosphere, *J. Geophys.*, 19,129–19,136, 1996.

Rosenlof, K. H., and J. R. Holton, Estimates of the stratospheric residual circulation using the downward control principle, *J. Geophys. Res.*, *98*, 10,465–10,479, 1993.

Sassi, F., D. Kinnison, B. A. Boville, R. R. Garcia, and R. Roble, The impact of variable sea-surface temperature on the circulation and thermal structure of the middle and upper atmosphere, *Eos Trans. AGU*, *82*(47), Fall Meet. Suppl., abstract SA51B-07, 2001.

Siskind, D. E., On the coupling between middle and upper atmospheric nitric oxide, in *Atmospheric Science Across the Stratopause*, *Geophys. Monogr. Ser.*, vol. 123, edited by D. E. Siskind et al., 2000.

Siskind, D. E., J. T. Bacmeister, M. E. Summers, S. E. Zasadil, and J. M. Russell, Two-dimensional model calculations of nitric oxide transport in the middle atmosphere and comparison with Halogen Occultation Experiment data, *J. Geophys. Res.*, *102*, 3527–3545, 1997.

Siskind, D. E., J. T. Bacmeister, and M. E. Summers, A new calculation of chemical eddy transport for several middle atmospheric tracers, *J. Geophys. Res.*, *103*, 31,321–31,329, 1998.

States, R. J., and C. S. Gardner, Thermal structure of the mesopause region (80–105 km) at 40N latitude, I, Seasonal variations, *J. Atmos. Sci.*, *57*, 66–92, 2000.

Summers, M. E., D. E. Siskind, J. T. Bacmeister, R. R. Conway, S. Zasadil, and D. F. Strobel, Seasonal variation of middle atmospheric $CH_4$ and $H_2O$ with a new chemical-dynamical model, *J. Geophys. Res.*, *102*, 3503–3526, 1997.

Summers, M. E., R. R. Conway, C. R. Englert, D. E. Siskind, M. H. Stevens, J. M. Russell III, L. L. Gordley, and M. J. McHugh, Discovery of a water vapor layer in the Arctic summer mesosphere: Implications for polar mesospheric clouds, *Geophys. Res. Lett.*, *28*, 3601–3604, 2001.

Thomas, G. E., and J. J. Olivero, The heights of polar mesospheric clouds, *Geophys. Res. Lett.*, *13*, 1403–1406, 1986.

Vincent, R. A., Gravity-wave motions in the mesosphere and lower thermosphere observed at Mawson, Antarctica, *J. Atmos. Terr. Phys.*, *56*, 593–602, 1994.

Wintersteiner, P. P., R. H. Picard, R. D. Sharma, J. R. Winick, and R. A. Joseph, Line-by-line radiative excitation model for the nonequilibrium atmosphere: Application to $CO_2$ 15 μm emission, *J. Geophys. Res.*, *97*, 18,083–18,117, 1992.

Woodman, R. F., et al., First observations of polar mesosphere summer echoes in Antarctica, *J. Geophys. Res.*, *104*, 22,577–22,590, 1999.

Yu, J. R., and C. Y. She, Climatology of a midlatitude mesopause region observed by a lidar at Fort Collins, Colorado (40.6N, 105W), *J. Geophys. Res.*, *100*, 7441–7452, 1995.

Zhu, X., M. E. Summers, and D. F. Strobel, Calculation of $CO_2$ 15 micron band atmospheric cooling rates by Curtis matrix interpolation of correlated-k coefficients, *J. Geophys. Res.*, *97*, 12,787–12,797, 1992.

M. J. Alexander, 3380 Mitchell Lane, Colorado Research Associates, Boulder, CO 80301, USA. (alexand@colorado-research.com)

J. T. Bacmeister, NASA Goddard Space Flight Center, Code 916, Greenbelt Rd., Greenbelt, MD 20771-0001, USA. (bacmj@janus.gsfc.nasa.gov)

S. D. Eckermann, J. P. McCormack, and D. E. Siskind, Naval Research Laboratory, Code 7640, 4555 Overlook Ave SW, Washington, D. C. 20375, USA. (eckerman@uap2.nrl.navy.mil; mccormack@uap2.nrl.navy.mil; siskind@uap2.nrl.navy.mil)